Korea-Australia Rheology Journal
Vol. 15, No. 4, December 2003 pp. 159-166

Numerical simulation of flow-induced birefringence in injection molded disk

Goang-Ding Shyu, Avraam I. Isayev and Ho-Sang Lee*[1]
Institute of Polymer Engineering, The University of Akron, Akron, OH 44325-0301, USA
[1]Department of Mechanical Design Engineering, Chungju National University, 123 Kumdan-ri, Iryu-myon, Chungju, Chungbuk 380-702, Korea

(Received June 19, 2003; final revision received August 27, 2003)

Abstract

This study is an attempt to understand the birefringence and stress development in an injection molded disk. A computer code was developed to simulate all three stages of the injection molding process filling, packing and cooling by finite element method. The constitutive equation used here was compressible Leonov model. The PVT relationship was assumed to follow the Tait equation. The flow-induced birefringence was related to the calculated flow stresses through the linear stress-optical law. The predicted birefringence was in good agreement with the experimental results.

Keywords **:** birefringence, viscoelasticity, injection molding, polystyrene

1. Introduction

Compact optical disks have become increasingly used for information storage in recent years (Ojima *et al.*, 1986; Takeshima *et al.*, 1986). The optical quality of molded parts is affected by the occurrence of frozen-in birefringence. The birefringence in molded parts is recognized to appear from two main sources (Isayev and Hieber, 1980; Isayev, 1983; 1987; 1991; Wimberger-Friedl, 1995). The first is flow-induced birefringence, which is a consequence of shear and normal stresses developing during cavity filling and leading to orientation of molecular chains. The second source of birefringence is nonequilibrium change of density and shrinkage, and the viscoelastic and photo-viscoelastic behavior of the polymer during the inhomogeneous rapid cooling through the glass transition temperature resulting in thermal birefringence. The birefringence of molded parts is a consequence of the interplay of these phenomena.

In the melt state, the flow-induced birefringence is related to the flow stresses through the well-known linear stress-optical rule (Janeschitz-Kriegl, 1983). The problem of flow-induced stresses and orientation is modeled on the basis of the nonlinear viscoelastic constitutive equation (Yu *et al.*, 1992; Famili *et al.*, 1991; Shyu *et al.*, 1995; Guo *et al.*, 1999; Kim *et al.*, 1999; Lee *et al.*, 2002; Chen *et al.*, 2002). Isayev and Hieber (1980) were among the first who proposed theoretical approach to relate the nonlinear viscoelasticity of polymers to the development of frozen-in molecular orientation (birefringence) in moldings.

Baaijens (1991) and Flaman (1993) used the compressible Leonov model, which is a nonlinear viscoelastic model, to simulate the injection molding cycle and the residual flow stresses for a strip mold.

Kwon *et al.*, (1999; 2002) developed a numerical analysis system using a finite difference method and studied the distribution of birefringence in a center-gated disk after injection molding and injection/compression molding processing using the Leonov model.

In this study, we have developed a numerical simulation program using finite element method for the injection molding of a center-gated disk, considering all three stages of the injection molding process filling, packing and cooling. The constitutive equation used here was compressible Leonov model (Shyu *et al.*, 1993). The PVT relationship was assumed to follow the Tait equation. Through the linear stress-optical law (Janeschitz-Kriegl, 1983), the flow-induced birefringence was related to the flow stresses calculated with Leonov model. The results of numerical simulation were compared with the corresponding experimental data (Yoon, 1995).

2. Theory

2.1. Governing equations

Very often the thickness of a cavity is much smaller than planar dimensions. Therefore, in a simulation of flow in a thin cavity, the velocity component in the gapwise direction is assumed to be equal to zero.

The momentum equations in the absence of inertia and body forces are:

*Corresponding author: lhs@gukwon.chungju.ac.kr

$$\frac{\partial \sigma_{xx}}{\partial x}+\frac{\partial \sigma_{xz}}{\partial z}=0 \tag{1}$$

$$\frac{\partial \sigma_{yy}}{\partial y}+\frac{\partial \sigma_{yz}}{\partial z}=0 \tag{2}$$

where x and y are planar directions and z is the gapwise direction, and σ represents the total stress.

The continuity equation for a compressible two-dimensional flow is:

$$\frac{\partial \rho}{\partial t}+\frac{\partial}{\partial x}(\rho v_x)+\frac{\partial}{\partial y}(\rho v_y)=0 \tag{3}$$

where v_x and v_y are velocity components in the x and y directions and the density ρ is assumed to follow the Tait equation:

$$\rho(P,T)=\rho_0(T)\left\{1-C\ln\left[1+\frac{P}{B(T)}\right]\right\}^{-1} \tag{4}$$

where C is a constant and B is a function of temperature.

In a nonisothermal problem, the momentum and the continuity equations are coupled with the energy equation. Since the transverse dimension in a thin cavity is much smaller than the planar dimensions, the thermal conductivity in the planar dimensions is ignored compared to that in the gapwise direction. Then the energy equation is:

$$\rho C_p\left(\frac{\partial T}{\partial t}+v_x\frac{\partial T}{\partial x}+v_y\frac{\partial T}{\partial y}\right)=\frac{\partial}{\partial z}\left(\kappa\frac{\partial T}{\partial z}\right)+\Phi \tag{5}$$

where C_p, κ and Φ are specific heat, thermal conductivity, and dissipation function, respectively. The dissipation function is given as

$$\Phi=2\eta_0 s\cdot tr\underline{\underline{e}}^2+\sum_k\frac{\eta_k}{4\theta_k^2}\left[\frac{I_1(I_2-I_1)}{3}+tr\underline{\underline{C}}_k^2-3\right] \tag{6a}$$

where $\underline{\underline{e}}=\frac{1}{2}(\nabla\underset{\sim}{v}+\nabla\underset{\sim}{v}^T)$. (6b)

$\underset{\sim}{v}$ is the velocity vector, I_1 and I_2 are the invariants of the elastic strain tensor $\underline{\underline{C}}_k$, and η_k, θ_k and s are described in the following paragraph.

By employing the Leonov constitutive model, the stress field can be related to the velocity gradient field as follows:

$$\underline{\underline{\sigma}}=-P\underline{\underline{\delta}}+\eta_0 s(\nabla\underset{\sim}{v}+\nabla\underset{\sim}{v}^T)+\sum_k\frac{\eta_k}{\theta_k}\underline{\underline{C}}_k \tag{7}$$

where P is the pressure, s is a rheological parameter lying between zero and one, and η_k and θ_k are the k^{th} mode shear viscosity and relaxation time, respectively, and C_k is the elastic strain tensor for the k^{th} mode of Leonov model.

The parameters η_k and θ_k are temperature dependent quantities based on a WLF temperature shift factor (Isayev, 1991), namely $\eta_k(T)=\eta_k(T_o)\cdot a_T/a_{To}$ and

$$\theta_k(T)=\theta_k(T_o)\cdot a_T/a_{To}$$

where

$$a_T=\begin{cases}a_{Tg} & T\le T_g\\ \exp\left[-\dfrac{C_1(T-T_{ref})}{C_2(T-T_{ref})}\right] & T>T_g\end{cases} \tag{8}$$

T_{ref} is the reference temperature, T_g is the glass transition temperature, and C_1 and C_2 are constants. The zero shear rate viscosity function η_0 is defined as

$$\eta_0=\sum_k\eta_k/(1-s)$$

In addition, $\underline{\underline{C}}_k$ is the elastic strain tensor of the k^{th} mode governed by

$$\frac{D}{Dt}\underline{\underline{C}}_k-\nabla\underset{\sim}{v}^T\cdot\underline{\underline{C}}_k-\underline{\underline{C}}_k\cdot\nabla\underset{\sim}{v}+\frac{1}{2\theta_k}(\underline{\underline{C}}_k\cdot\underline{\underline{C}}_k-\underline{\underline{\delta}})=0 \tag{9}$$

where $\frac{D}{Dt}\underline{\underline{C}}_k$ is the substantial derivative of $\underline{\underline{C}}_k$ with respect to time.

$$\frac{D}{Dt}\underline{\underline{C}}_k=\frac{\partial}{\partial t}\underline{\underline{C}}_k+\underset{\sim}{v}\cdot\nabla\underline{\underline{C}}_k \tag{10}$$

2.2. Numerical formulations

Solution of the governing equations with a set of appropriate boundary conditions provides the velocity and the pressure profiles. The boundary of a cavity during flow consists of a melt front, impermeable boundaries, and a gate. In the melt front, one may assume that the pressure is equal to zero and can use this as a reference pressure. In the impermeable boundary region, the melt is in contact with the boundary of the mold or insert, and the normal velocity components vanish. The flow rate is usually specified at the gate or at the entry. In addition, symmetry boundary conditions at the centerline and no slip velocity at the solid wall of the cavity are assumed. Thus, the boundary conditions may be summarized as:

$$v_x=v_y=0 \text{ at } z=h \tag{11}$$

$$\frac{\partial v_x}{\partial z}=\frac{\partial v_y}{\partial z}=0 \text{ at } z=0 \tag{12}$$

$$P=0 \text{ at the melt front} \tag{13}$$

$$Q=Q_0 \text{ at the gate or entry} \tag{14}$$

Other boundary conditions on temperature are:

$$T=T_w \text{ at } z=h \tag{15}$$

$$\frac{\partial T}{\partial z}=0 \text{ at } z=0 \tag{16}$$

By substituting Eq. (7) into the Eq. (1) and (2), and integrating the results with respect to z and using the symmetric boundary conditions, Eq. (12), the velocity gradients in the absence of normal forces are:

$$\frac{\partial v_x}{\partial z}=\frac{\partial P}{\partial x}\frac{z}{\eta_x} \tag{17}$$

$$\frac{\partial v_y}{\partial z} = \frac{\partial P}{\partial y}\frac{z}{\eta_y} \tag{18}$$

where:

$$\eta_x = \eta_0 s + \frac{1}{\frac{\partial v_x}{\partial z}}\sum_k \frac{\eta_k}{\theta_k} C_{xz,k} \tag{19}$$

$$\eta_y = \eta_0 s + \frac{1}{\frac{\partial v_y}{\partial z}}\sum_k \frac{\eta_k}{\theta_k} C_{yz,k} \tag{20}$$

Integration of Eq. (17) and (18), using Eq. (11), leads to:

$$v_x = -\frac{\partial P}{\partial x}\int_z^h \frac{z'}{\eta_x} dz' \tag{21}$$

$$v_y = -\frac{\partial P}{\partial y}\int_z^h \frac{z'}{\eta_y} dz' \tag{22}$$

With substitution of Eq. (21) and (22) into the Eq. (3), the governing equation for pressure is:

$$G\frac{\partial P}{\partial t} + H - \frac{\partial}{\partial x}\left(S_x \frac{\partial P}{\partial x}\right) - \frac{\partial}{\partial y}\left(S_y \frac{\partial P}{\partial y}\right) = 0 \tag{23}$$

where:

$$G = \int_0^h \left(\frac{\partial \rho}{\partial P}\right) dz \tag{24}$$

$$H = \int_0^h \left(\frac{\partial \rho}{\partial T}\right)\left(\frac{\partial T}{\partial t}\right) dz \tag{25}$$

$$S_x = \int_0^h \left(z\int_0^z \rho dz'\right)\frac{dz}{\eta_x} \tag{26}$$

$$S_y = \int_0^h \left(z\int_0^z \rho dz'\right)\frac{dz}{\eta_y} \tag{27}$$

The control-volume finite element method (Wang *et al.*, 1986; Isayev, 1991) with triangular elements and linear shape functions is used to solve Eq. (23), with G and H taken to be constant in each control volume, S_x and S_y to be constant in each element. As it is seen, in the simulations governing transfer equations are calculated in Cartesian coordinate. However, to avoid cumbersome numerical calculations, constitutive equation is solved in cylindrical streamwise coordinate as shown below.

2.3. Determination of the elastic strain tensor and birefringence

For general planar geometries, the elastic strain tensor is determined in the streamwise coordinate system (r, θ, z), where r is the flow direction, θ is perpendicular to r in the counterclockwise direction, and z is in the gapwise direction. The shear component $C_{\theta z}$ and C_{rz} are assumed to be zero. From Eq. (9), the governing equations for the elastic strain tensor in the streamwise coordinate system are

$$\frac{\partial C_{rr,k}}{\partial t} + v_r \frac{\partial C_{rr,k}}{\partial r} = 2\left(-\frac{v_r}{r}\right)C_{rr,k} + 2C_{zr,k}\dot{\gamma} - \frac{1}{2\theta_k}\left(C_{rr,k}^2 + C_{zr,k}^2 - 1 + \frac{A}{3}C_{rr,k}\right) \tag{28}$$

$$\frac{\partial C_{rz,k}}{\partial t} + v_r \frac{\partial C_{rz,k}}{\partial r} = -\frac{v_r}{r}C_{rz,k} + C_{zz,k}\dot{\gamma} - \frac{1}{2\theta_k}\left[(C_{rr,k} + C_{zz,k})C_{rz,k} + \frac{A}{3}C_{rz,k}\right] \tag{29}$$

$$\frac{\partial C_{zz,k}}{\partial t} + v_r \frac{\partial C_{zz,k}}{\partial r} = -\frac{1}{2\theta_k}\left(C_{zr,k}^2 + C_{zz,k}^2 - 1 + \frac{A}{3}C_{zz,k}\right) \tag{30}$$

$$\frac{\partial C_{\theta\theta,k}}{\partial t} + v_r \frac{\partial C_{\theta\theta,k}}{\partial r} = 2\frac{v_r}{r}C_{\theta\theta,k} - \frac{1}{2\theta_k}\left(C_{\theta\theta,k}^2 - 1 + \frac{A}{3}C_{\theta\theta,k}\right) \tag{31}$$

$$C_{zz,k} = \left(\frac{1}{C_{\theta\theta,k}} + C_{rz,k}^2\right)/C_{rr,k} \tag{32}$$

$$A = (C_{\theta\theta,k} - 1)\left(C_{rr,k} + C_{zz,k} - 1 - \frac{1}{C_{\theta\theta,k}}\right) \tag{33}$$

where :

$$\dot{\gamma} = \frac{\partial v_r}{\partial z} = \sqrt{\left(\frac{\partial v_x}{\partial z}\right)^2 + \left(\frac{\partial v_y}{\partial z}\right)^2} \tag{34}$$

$$v_r = \frac{\partial P}{\partial r}\int_z^h \frac{z'}{\eta_r} dz' \tag{35}$$

$$\eta_r = \eta_0 s + \frac{1}{\dot{\gamma}_k}\sum_k \frac{\eta_k}{\theta_k} C_{rz,k} \tag{36}$$

The values of C_k at the entrance node are determined from the fully developed steady-state solution, $\frac{DC_k}{Dt} = 0$, under isothermal conditions. C_{rr}, C_{rz}, C_{zz} and $C_{\theta\theta}$ together with $\dot{\gamma}$ and $\frac{\partial P}{\partial r}$ are then determined from the governing equations by numerical integration with all integrals by trapezoidal quadrature (Sobhanie *et al.*, 1989).

The flow-induced birefringence in the rz plane can be calculated, according to the stress-optical law being

$$\Delta n = C_o^{\eta}\sqrt{(\sigma_{rr} - \sigma_{zz})^2 + 4\tau_{rz}^2} \tag{37}$$

where C_o^{η} is the stress-optical coefficient at the melt state.

3. Results and discussion

The simulation was based on the experiment of Yoon (1995). The material used is polystyrene (Styron 615APR/DOW), and the mold is a center-gated disk. The diameter and thickness of the disk is 10.16 cm and 0.2 cm, respectively. The molding conditions are as follows: melt temperature is 225°C, mold temperature is 40°C, and volumetric flow rate is 23.8 cm^3/s. The material data for PS used in the simulation are given in Table 1 (Shyu, 1993). 315 elements with 184 nodes are used for the quarter disk, considering symmetry of the disk. The finite element meshes together with the location of the gate are shown in Fig. 1.

RESULTS AND DISCUSSION

Sequence of apoLp-III gene from *H. cunea* and sequence comparisons with other apoLp-III

Figure 1 shows the cDNA sequence of apoLp-III from *H. cunea*. Using degenerate primers designed from the internal consensus sequences, a 320 bp fragment of apoLp-III was amplified from RNA of adult whole body by RT-PCR. In an attempt to obtain the 5- and 3- ends of coding sequence, 5- and 3-RACE PCRs were performed using gene specific primers. The apoLp-III cDNA has a length

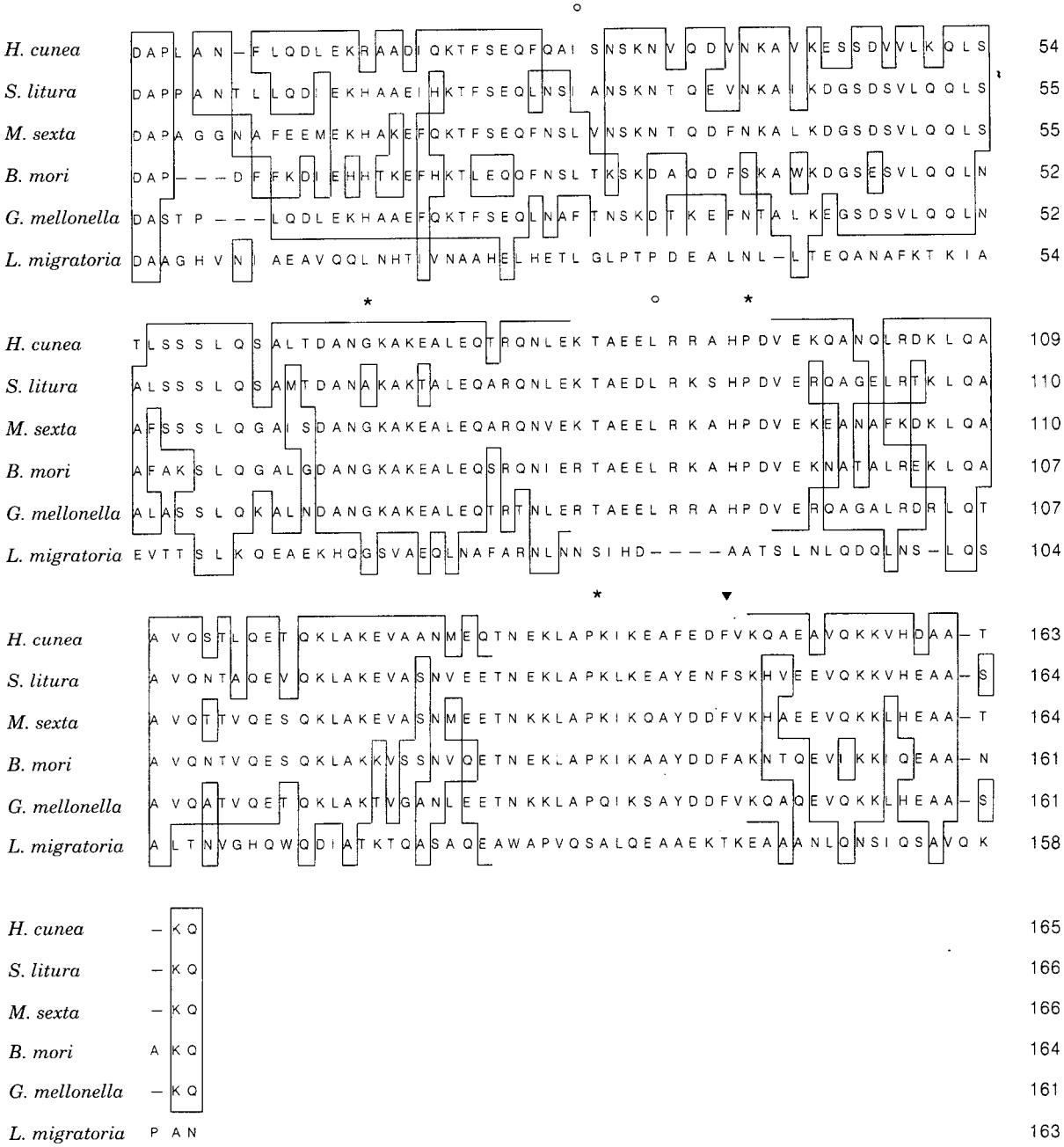

Fig. 1. Alignment of the amino acid sequences of insect apoLp-IIIs. Aligned amino acid sequences for apoLp-IIIs from *Spodoptera litura* (AF094582), *Manduca sexta* (M17286), *Bombyx mori* (U59244), *Galleria mellonella* (P80703), and *Locusta migratoria* (J03888). The leucines that are putatively involved in the initial contact with the lipophorin surface are indicated by circle. Conserved residues that are probably involved in breaks and/or turns between helices are marked by asterisks. The phenylalanine that may contribute to structural stability of α-helix is indicated by triangle. Identical residues and conservative replacements in apoLp-III are in box.

0.07 second and the temperature is still high. Later, when the temperature becomes low and the relaxation time enlarges (meaning that the induced stresses will not relax right away), the normal stresses near the midplane grow again although the flow becomes even smaller. It is noted that the normal stresses near the cavity wall does not change during the packing stage, since the temperature near the cavity wall is lower than the glass transition temperature so that the stresses have been frozen.

The predicted transient development of the second normal stress difference $\sigma_{\theta\theta} - \sigma_{zz}$ in the filling and packing stages is shown in Fig. 5 and 6, respectively. The shape of the distribution of $\sigma_{\theta\theta} - \sigma_{zz}$ is similar to that of the first normal stress difference $\sigma_{rr} - \sigma_{zz}$, but the value of $\sigma_{\theta\theta} - \sigma_{zz}$ are one order of magnitude smaller than those of $\sigma_{rr} - \sigma_{zz}$.

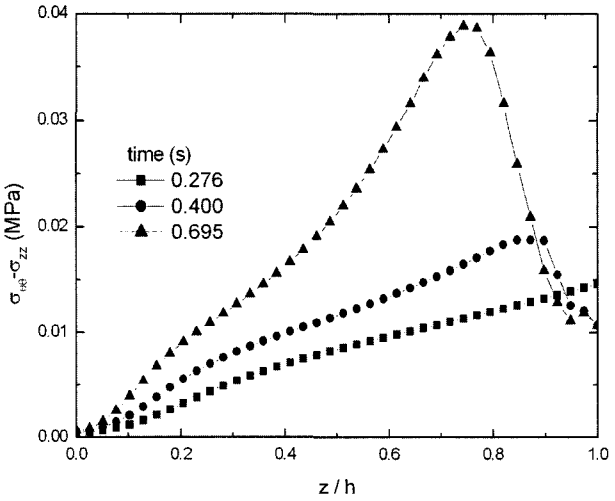

Fig. 5. Predicted transient gapwise distributions of the second normal stress difference ($\sigma_{\theta\theta} - \sigma_{zz}$) at $r = 3.07$ during filling stages.

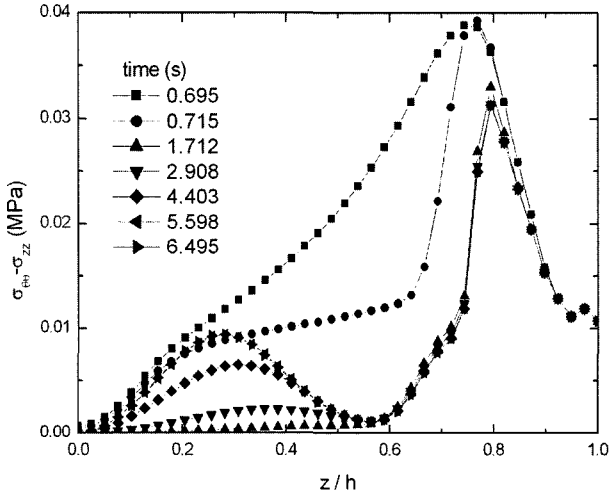

Fig. 6. Predicted transient gapwise distributions of the second normal stress difference ($\sigma_{\theta\theta} - \sigma_{zz}$) at $r = 3.07$ during packing stages.

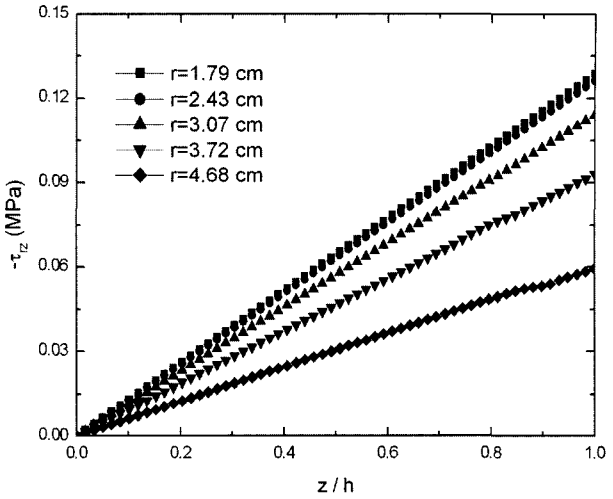

Fig. 7. Predicted gapwise distribution of shear stress τ_{rz} at various radial positions at the end of filling ($t = 0.694$ s).

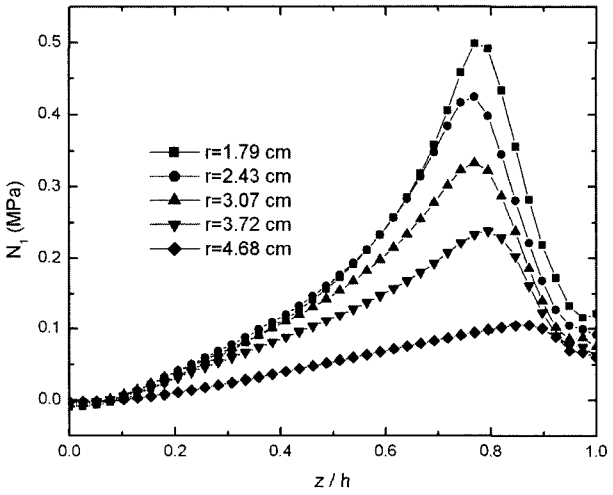

Fig. 8. Predicted gapwise distribution of the first normal stress difference N_1 at various radial positions at the end of filling (t = 0.694 s).

Fig. 7 represents the gapwise distributions of shear stress at various radial positions. Shear stress has an almost linear gapwise distribution with a slope depending on the proximity to the melt.

Fig. 8 shows the gapwise distribution of the first normal stress difference at various radial positions at the end of filling. The peaks continually decrease in magnitude and move toward the wall with increasing radial positions from the gate.

The predicted gapwise flow birefringence distribution at various radial positions at the end of filling stage is shown in Fig. 9. The birefringence shows a maximum around $z/h \cong 0.7$~0.8, like the first normal stress difference. It is noted that although the shear stress varies monotonically with z, the birefringence exhibits a peak away from the wall, due to the dominant effect of the first normal stress

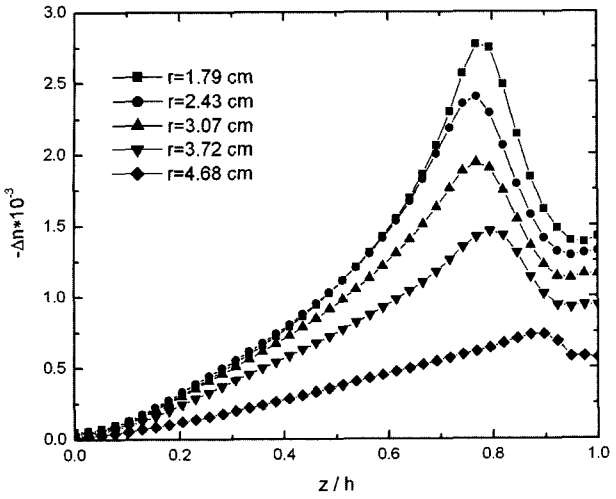

Fig. 9. Predicted gapwise distribution of birefringence Δn at various radial positions at the end of filling ($t = 0.694$ s).

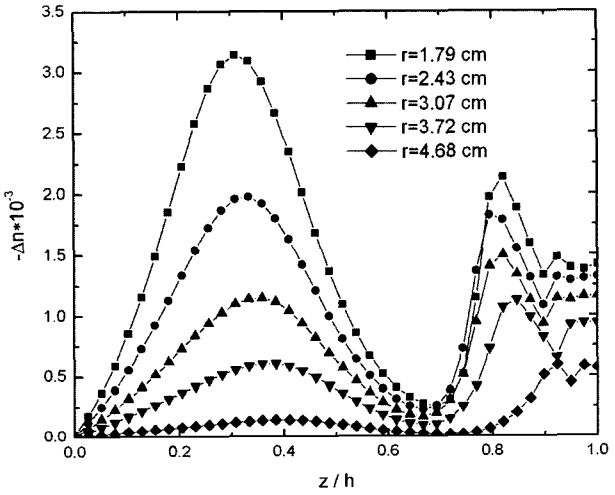

Fig. 10. Predicted gapwise distribution of birefringence Δn radial positions at the end of packing ($t = 6.74$ s).

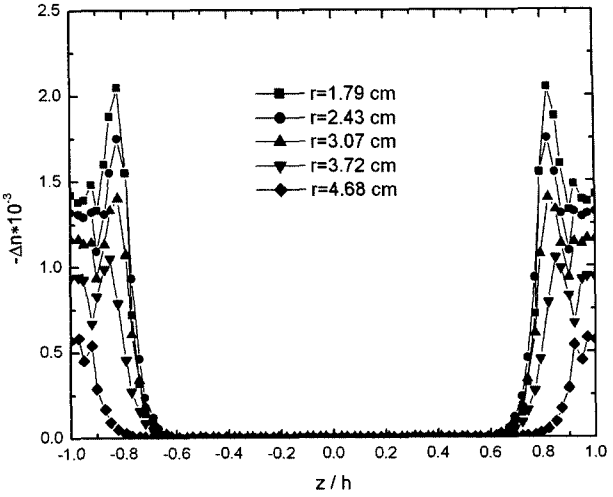

Fig. 11. Predicted gapwise distribution of birefringence Δn at various radial positions at the end of cooling when no packing pressure is applied.

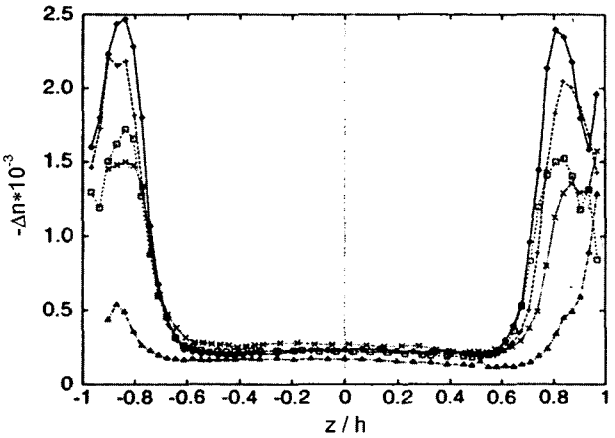

Fig. 12. Measured gapwise distribution of birefringence Δn at various radial positions at the end of cooling when no packing pressure is applied.

difference.

The predicted gapwise birefringence distribution at various radial positions at the end of packing stage with a packing pressure of 15 MPa are shown in Fig. 10. There are two peaks in the birefringence distribution; one near the surface produced in the filling stage, the other near the center produced by the additional flow in the packing stage. The inner peak also decreases in magnitude as the radial position increases from the gate.

Without the packing stage, the predicted flow birefringence distributions at the end of cooling stage are given in Fig. 11. The flow-induced birefringence at the core is zero due to the fast relaxation of the chain orientation right after filling. Fig. 12 is the corresponding experimental results measured by Yoon (1995). It is seen that the simulation, in good agreement with the experimentation, shows appreciable birefringence at the wall and a peak which moves toward the wall with increasing radial positions from the gate. One thing to be noted is that birefringence at the center line is zero in simulation whereas experimental data indicate that a certain degree of birefringence exists around the center line. The possible reason for the difference is thermally induced residual stress is built up in the molded part including the centerline of the cavity as shown by Isayev (1983).

The predicted and experimental gapwise birefringence distributions at the end of cooling stage with a packing pressure of 15 MPa are presented in Fig. 13 and 14, respectively. The predicted birefringence is in good agreement with the experimental results such as the locations and magnitude of the inner peaks. However, some differences exist, such as the minimum value in the troughs, and the magnitude near the surface. Possible reasons may be due to inaccuracy in shift factors for viscosity and relaxation time

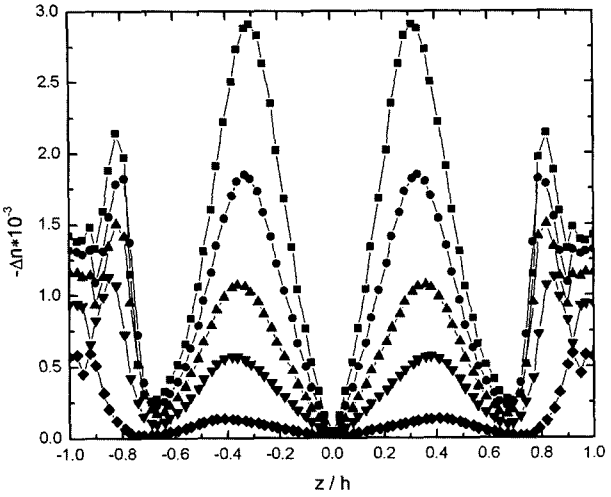

Fig. 13. Predicted gapwise distribution of birefringence Δn at various radial positions at the end of cooling with packing pressure of 15 MPa.

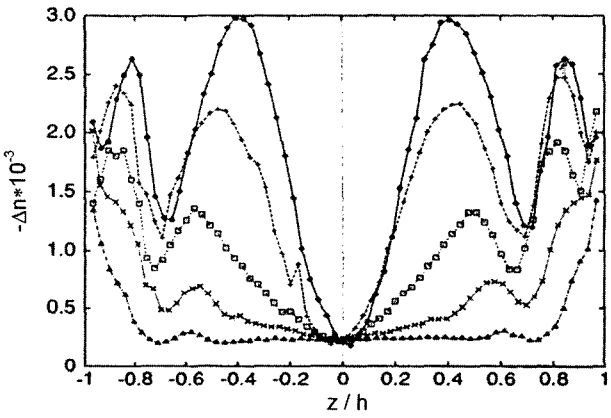

Fig. 14. Measured gapwise distribution of birefringence Δn at various radial positions at the end of cooling with packing pressure of 15 MPa.

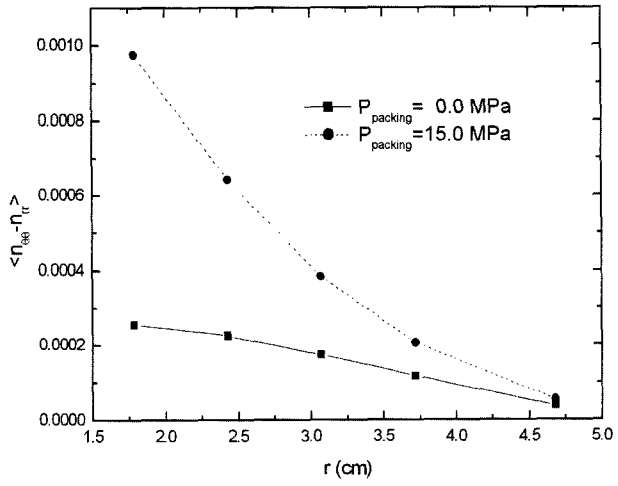

Fig. 15. Predicted radial profiles of gapwise-averaged residual birefringence $\langle n_{\theta\theta} - n_{rr} \rangle$ with packing pressures of 0 and 15 MPa, respectively.

at low temperatures.

The radial dependence of gapwise-averaged birefringence $\langle n_{\theta\theta} - n_{rr} \rangle \left(= \frac{1}{h}\int_0^h (n_{\theta\theta} - n_{rr}) dz \right)$ is shown in Fig. 15. $\langle n_{\theta\theta} - n_{rr} \rangle$ is a monotonously decreasing function of radial position. Similar data have been reported by Greener (1989). It is seen from the simulation results that packing makes $\langle n_{\theta\theta} - n_{rr} \rangle$ increase significantly near the gate. Since there is less and slower material flow at larger radial positions in the packing stage, a smaller increase in $\langle n_{\theta\theta} - n_{rr} \rangle$ at larger radial position due to packing is obtained.

4. Conclusions

A computer code which used the compressible Leonov model was developed to simulate the injection molding cycle. The simulation was verified with corresponding experimental measurements (Yoon, 1995) of pressure traces, gapwise flow-induced birefringence in center- gated disk. The simulation showed that

(1) The predicted birefringence was in good agreement with the experimental results such as the locations and magnitude of the peaks.

(2) When the packing pressure of 15 MPa was applied, there were two peaks in the birefringence distribution; one near the surface produced in the filling stage, the other near the center produced by the additional flow in the packing stage. The inner peak decreased in magnitude as the radial position increased from the gate.

(3) With the packing pressure, gapwise-averaged birefringence increased significantly near the gate. However, increment of the birefringence at larger radial position was small, since there was less and slower material flow at larger radial positions in the packing stage.

Acknowledgement

The authors greatly appreciate the financial support of the National Science Foundation Division of Engineering (DMI-0322920).

References

Baaijens, F.P.T., 1991, Calculation of residual stresses in injection molded products, *Rheol. Acta* **30**, 284-299.

Chen, S.C., Y.C. Chen and H.S. Peng, 2002, Simulation of injection-compression molding process, Part 3: Effect of process conditions on part birefringence, *Advances in Polymer Technology* **21**, 177-187.

Famili, N. and A.I. Isayev, 1991, in Modeling of polymer processing: Recent developments, Hanser, Munich.

Flaman, A.A., 1993, Buildup and relaxation of molecular orientation in injection molding. Part I: Formulation, *Polym. Eng. Sci.* **33**, 193-201.

Greener, J., R. Kesel and B.A. Contestable, 1989, The bire-

fringence problem in optical disk substrates: A modeling approach, *AIChE J.* **35**, 449-458.

Guo, X. and A.I. Isayev, 1999, Residual stresses and birefringence in injection molding of semicrystalline polymer, *Int. Polym. Process.* **14**, 387-398.

Isayev, A.I., 1983, Orientation development in the injection molding of amorphous polymers, *Polym. Eng. Sci.* **23**, 271-284.

Isayev, A.I., Ed., 1991, Modeling of polymer processing: Recent development, Hanser, Munich.

Isayev, A.I. and C.A. Hieber, 1980, Toward a viscoelastic modeling of the injection molding of polymers, *Rheol. Acta* **19**, 168-182.

Isayev, A.I., Ed., 1987, Injection and compression molding fundamentals, Marcel Dekker, New York.

Janeschitz-Kriegl H., 1983, Polymer melt rheology and flow birefringence, Springer, Berlin.

Kim, I.H., S.J. Park, S.T. Chung and T.H. Kwon, 1999, Numerical modeling of injection/compression molding for center-gated disk: Part 1. Injection molding with viscoelastic compressible fluid model, *Polym. Eng. Sci.* **39**, 1930-1942.

Lee, Y.B., T.H. Kwon and K. Yoon, 2002, Numerical prediction of residual stresses and birefringence in injection/compression molded center-gated disk. Part 1: Basic modeling and results for injection molding, *Polym. Eng. Sci.* **42**, 2246-2272.

Ojima, M., A. Saito, T. Kaku, M. Ito, Y. Tsunoda, S. Takayama and Y. Sugita, 1986, Compact magnetooptical disk for coded data storage, *Appl. Optics* **25**, 483-489.

Shyu, G.D., 1993, Birefringence and residual stresses in molded articles of amorphous polymers, Ph.D. Dissertation, The University of Akron.

Shyu, G.D. and A.I. Isayev, 1995, Residual stresses and birefringence in injection molded disks, SPE ANTEC Tech Papers **41**, 2911-2917.

Sobhanie, M. and A.I. Isayev, 1989, Viscoelastic simulation of flow of rubber compounds, *Rubb. Chem. Tech.* **62**, 939-956.

Takeshima, M. and N. Funakoshi, 1986, Molecular orientation distribution in injection-molded polycarbonate discs, *J. Appl. Polym. Sci.* **32**, 3457-3468.

Wang, V.W., C.A. Hieber and K.K. Wang, 1986, Dynamic simulation and graphics for the injection molding of three-dimensional thin parts, *J. Polym. Eng.* **7**, 21-45.

Wimbereger-Friedl R., 1995, Assessment of orientation, stress and density distributions in injection-molded amorphous polymers by optical techniques, *Prog. Polym. Sci.* **20**, 369-401.

Yoon, K., 1995, An experimental study on precision injection molding of center-gated disks, *Korean J. of Rheol.* **7**, 19-27.

Yu, J.S., A.H. Wagner and D.M. Kalyon, 1992, Simulation of microstructure development in injection molding of engineering plastics, *J. Appl. Polym. Sci.* **44**, 477-489.